

Atmospheric Origins of Variability in the South Atlantic Meridional Overturning Circulation

TIMOTHY SMITH AND PATRICK HEIMBACH^a

Institute for Computational Engineering and Sciences, The University of Texas at Austin, Austin, Texas

(Manuscript received 5 June 2018, in final form 5 November 2018)

ABSTRACT


Insights from the RAPID–MOCHA observation network in the North Atlantic have motivated a recent focus on the South Atlantic, where water masses are exchanged with neighboring ocean basins. In this study, variability in the South Atlantic meridional overturning circulation (SAMOC) at 34°S is attributed to global atmospheric forcing using an inverse modeling approach. The sensitivity of the SAMOC to atmospheric state variables is computed with the adjoint of the Massachusetts Institute of Technology general circulation model, which is fit to 20 years of observational data in a dynamically consistent framework. The dynamical pathways highlighted by these sensitivity patterns show that the domain of influence for the SAMOC is broad, covering neighboring ocean basins even on short time scales. This result differs from what has previously been shown in the North Atlantic, where Atlantic meridional overturning circulation (AMOC) variability is largely governed by dynamics confined to that basin. The computed sensitivities are convolved with surface atmospheric state variability from ERA-Interim to attribute the influence of each external forcing variable (e.g., wind stress, precipitation) on the SAMOC from 1992 to 2011. Here, local wind stress perturbations are shown to dominate variability on seasonal time scales while buoyancy forcing plays a minor role, confirming results from past forward perturbation experiments. Interannual variability, however, is shown to have originated from remote locations across the globe, including a nontrivial component originating from the tropical Pacific. The influence of atmospheric forcing emphasizes the importance of continuous widespread observations of the global atmospheric state for attributing observed AMOC variability.


1. Introduction

The Atlantic meridional overturning circulation (AMOC) provides a convenient metric for ocean circulation as contributions from boundary currents, geostrophic flow, and wind-driven transport are integrated to one quantity of meridional volumetric transport. Most studies have focused on variability of the AMOC in the

Northern Hemisphere, where the main AMOC observing systems are located, in particular the RAPID–MOCHA array at 26.5°N (Cunningham et al. 2007; Rayner et al. 2011) and the recently implemented Overturning in the Subpolar North Atlantic Program (OSNAP; Lozier et al. 2017). Results from these monitoring systems have motivated a new focus on the meridional overturning circulation (MOC) in the South Atlantic, where observations are sparse in comparison, thus prompting the South Atlantic meridional overturning circulation (SAMOC) initiative (SAMOC Initiative 2017).

The South Atlantic Ocean plays an active role in exchanging water masses from neighboring ocean basins and transforming them into the relatively warm, salty waters that are transported northward as part of the upper limb of the AMOC (Garzoli and Matano 2011). Indeed, the region has a unique net equatorward heat transport, which is strongly correlated with the AMOC (Dong et al. 2009), indicating that the interocean water mass exchanges that occur here are crucial for global ocean circulation and heat transport (Garzoli et al. 2013). However, variability in

 Denotes content that is immediately available upon publication as open access.

 Supplemental information related to this paper is available at the Journals Online website: <https://doi.org/10.1175/JCLI-D-18-0311.s1>.

^aAdditional affiliations: Institute for Computational Engineering and Sciences, and Jackson School of Geosciences, and Institute for Geophysics, The University of Texas at Austin, Austin, Texas.

Corresponding author: Timothy Smith, tsmith@ices.utexas.edu

DOI: 10.1175/JCLI-D-18-0311.1

© 2019 American Meteorological Society. For information regarding reuse of this content and general copyright information, consult the [AMS Copyright Policy](#) (www.ametsoc.org/PUBSReuseLicenses).

the region is not well understood, as there are no direct measurements of the SAMOC extending longer than a decade. Here, we perform a sensitivity analysis to highlight the ocean dynamics that communicate variability originating in the atmosphere to the SAMOC, generating variability on seasonal to interannual time scales.

We focus our attention on the variability of the AMOC at 34°S to capture interocean exchanges that occur here (Anson et al. 2014). We use the Massachusetts Institute of Technology general circulation model (MITgcm) fit to observational data from 1992 to 2011 through the state estimation procedure developed by the consortium for Estimating the Circulation and Climate of the Ocean (ECCO; Forget et al. 2015a; Wunsch and Heimbach 2013a). Using the adjoint modeling framework developed within ECCO, we compute the gradient of the AMOC at 34°S to perturbations in atmospheric forcing (see section 2d). In the forward sense, sensitivities can be computed by mapping perturbations in each atmospheric forcing variable at each point in space to the AMOC via the model Jacobian. The adjoint operator is simply the transpose of the model Jacobian, mapping the influence from a single quantity onto the sources through the transposed or reversed model dynamics. The resulting sensitivity maps therefore elucidate the linearized dynamics that carry perturbations to the latitude band where the AMOC is evaluated. In the context of observing variability, this procedure allows us to quantify the impact each atmospheric state field has on SAMOC variability. This technique is extremely useful in a region where complex water mass exchanges make it difficult to tease out the underlying dynamics that communicate atmospheric perturbations to the South Atlantic.

Many previous studies have used this technique to attribute variability in the North Atlantic MOC (e.g., Marotzke et al. 1999; Bugnion et al. 2006; Czeschel et al. 2010; Heimbach et al. 2011). More recently, Pillar et al. (2016) used the MITgcm adjoint to attribute AMOC variations in the subtropical North Atlantic to atmospheric forcing perturbations. The authors showed that wind stress dominates AMOC variability on time scales shorter than a year, thermal forcing generates low-frequency variability, and that freshwater fluxes provide little contribution to the overall signal.

In this study, we follow a similar approach to Pillar et al. (2016) to investigate oceanic teleconnections relevant for communicating variability to the AMOC at 34°S. Here, we use the adjoint model associated with the ECCO, version 4, release 2, state estimate, which provides a number of advantages discussed in section 2a. The paper is laid out as follows: We discuss the numerical model, relevant parameterizations, and SAMOC variability in section 2. In section 3, we discuss the sensitive regions and time scales for communicating perturbations to 34°S. We then use

these sensitivities to reconstruct the 20-yr SAMOC signal in section 4 and show the global origins of seasonal and interannual variability in sections 5 and 6, respectively. Concluding remarks are discussed in section 7.

2. Experimental setup

a. Model configuration

In this study, we use the MITgcm, solving the hydrostatic, Boussinesq equations (Marshall et al. 1997) with a thermodynamic/dynamic sea ice model (Menemenlis et al. 2005; Losch et al. 2010; Heimbach et al. 2010). The model is specifically configured following the state estimation procedure of ECCO, version 4, release 2 (ECCOv4r2), which is described in greater detail in Forget et al. (2015a, 2016). The computational domain is the global ocean with a horizontal grid resolution of approximately $1^\circ \times 1^\circ$ (with refinements near the equator) and 50 vertical depth levels. Vertical mixing is parameterized as a function of turbulent kinetic energy as in Gaspar et al. (1990), along with a simple convective adjustment scheme. Unresolved eddies are parameterized with a bolus velocity following Gent and McWilliams (1990) and isopycnal diffusivity following Redi (1982).

The near-surface values for downward longwave and shortwave radiation, precipitation, specific humidity, air temperature, and wind stress vector at 6-h increments from ERA-Interim (Dee et al. 2011) are used as first-guess boundary conditions in the forward model. Air-sea fluxes (including evaporation) are computed based on these atmospheric state variables with the bulk formulas (Large and Yeager 2004), and continental runoff is provided as a seasonal climatology from Fekete et al. (2002).

We are motivated to use the ECCOv4r2 estimate specifically because it provides a dynamically consistent ocean state estimate, which is as close to observations as possible through the solution of an optimization problem. Forget et al. (2015a, Figs. 9, 10 therein) show that this state estimate has a substantially improved fit to hydrographic data compared to past estimates, including the eddy-permitting, Green's function-calibrated global cubed-sphere simulation, referred to as ECCO2 (Menemenlis et al. 2005), as a result of inverting for optimal turbulent transport coefficients (Forget et al. 2015b). Additionally, the ECCO framework allows for scalable computation of sensitivity patterns through the adjoint model, a unique feature of the underlying model that is essential for this study.

The uncertain three-dimensional parameter fields for each subgrid mixing scheme, initial conditions, and two-dimensional biweekly adjustments to the near-surface atmospheric state are computed within the nonlinear least squares optimization problem. In practice, convergence is

improved by separating the optimization into two phases. First, the parameter fields and initial conditions for temperature and salinity are computed through an optimization problem conditioned only on the temporal mean and seasonal variability of Argo data. The inferred model parameters generate a relative steady state for the model, substantially reducing artificial drift. Next, initial velocities are computed via a short forward integration that produces a mostly geostrophically balanced velocity field, given the adjusted initial hydrography. Finally, the full optimization infrastructure is deployed. Here, the final values of all the parameters, initial conditions, and atmospheric adjustments are the result of nonlinear optimization conditioned on all observational datasets described in Forget et al. (2015a) as part of the ECCO inverse modeling/optimization approach; see also Wunsch and Heimbach (2007).

The ECCO-adjusted forcing fields provide an atmospheric state from 1992 to 2011. We prepend this forcing record with adjusted ERA-Interim fields from 1979 to 1991 in order to have the longest record possible for the SAMOC reconstructions shown in sections 4–6. Details on generating these fields are given in the appendix.

b. The MOC at 34°S

The domain of interest is the zonal cross section of the Atlantic Ocean at 34°S, from the Argentine Basin in the west to the Cape of Good Hope Basin in the east. To simplify notation, we use Cartesian coordinates and denote the zonal coordinate between these two boundaries $x \in [x_W, x_E]$, the meridional coordinate $\{y: \phi = 34^\circ\text{S}\}$, and depth $z \in [-H, \eta(y, t)]$ (spherical coordinates are used in the computation, however). The meridional overturning streamfunction is defined as follows:

$$\psi_{\text{MOC}}(y, z, t) = - \int_{-H}^z \int_{x_W}^{x_E} v(x, y, z, t) dx dz, \quad (1)$$

so that the upper limb, northward volumetric transport is positive and the AMOC at latitude y is

$$\text{AMOC}(y, z_{\text{max}}, t) = \max_{-H < z < \eta(y, t)} \psi_{\text{MOC}}(y, z, t). \quad (2)$$

We use monthly mean values for meridional velocity v to filter out any higher-frequency variability.

c. Assessment of the ECCO state estimate

The SAMOC at 34°S diagnosed from ECCOv4r2 over 1992–2011 has a 20-yr mean of 14.3 ± 3.1 Sv ($1 \text{ Sv} \equiv 10^6 \text{ m}^3 \text{ s}^{-1}$), and a mean maximizing depth of 1422 m. The inclusion of the eddy bolus velocity (Gent and McWilliams 1990) in Eq. (1) leads to a strengthening and shoaling of the AMOC, resulting in a time mean of 16.1 ± 3.2 Sv at 1397 m. Compared to recent work in

the South Atlantic, these estimates are weaker than what is reported by studies based on in situ observations and proxies, including inferences from XBT lines (17.9 ± 2.2 Sv, Dong et al. 2009; 18.1 ± 2.3 Sv, Garzoli et al. 2013), Argo float data (18.4 Sv, Dong et al. 2014), sea surface height proxies (19.5 ± 3.5 Sv, Dong et al. 2015), or the brief 20-month record from two pilot mooring arrays taken during the time period analyzed here (21.3 ± 8.7 Sv, Meinen et al. 2013). Nevertheless, the time-mean transport is consistent to one standard deviation with that of Dong et al. (2011), who report 15.0 ± 3.7 Sv based on a $0.2^\circ \times 0.2^\circ$ horizontal resolution simulation covering 1980–96 with the Ocean General Circulation Model for the Earth Simulator (OFES). Here, we focus on the physical mechanisms that generate seasonal to interannual variability rather than time-mean processes.

The seasonal cycle of the SAMOC from ECCOv4r2, observations, and proxies is shown in Fig. 1c. The amplitude of the ECCOv4r2 estimate is close to that derived from Argo floats and Scatterometer Climatology of the Winds (SCOW) fields (Dong et al. 2014) and that from altimetric sea surface height proxies and NCEP-2 wind fields (Dong et al. 2015). The peak-to-peak amplitude from each is 7.5, 6.4, and 8.4 Sv, respectively. The phase of the ECCOv4r2 estimate is delayed by one month compared to these estimates, however, because of a relatively weaker amplitude in the seasonal cycle of the geostrophic component (Fig. 1b). Specifically, in comparison to the Argo observations, the phase of the geostrophic current in ECCOv4r2 matches, but the amplitude is 3.5 Sv weaker. Further comparison between ECCOv4r2- and Argo-derived density profiles are shown in Fig. 2, where the figures in Dong et al. (2014) are reproduced. The profiles show that the mismatch between the Argo and ECCOv4r2 geostrophic currents are due to subtle differences in the density fields, while the large-scale features are captured very well as a result of the data constraints in the ECCO optimization. The general agreement between the density and temperature fields provides confidence to use the ECCOv4r2 model, especially when compared to the performance of unconstrained models (Dong et al. 2014).

The interannual variability exhibited in the SAMOC and meridional heat transport (MHT) computed by ECCOv4r2 is shown in Fig. 1d as monthly values with the seasonal cycle and 20-yr time mean removed. The signals resemble Gaussian stochastic processes as noted in Wunsch and Heimbach (2013b). However, there is a slight strengthening in the early 2000s and a weak decreasing trend from roughly 2007 to 2011 (which are highlighted in the annual averages in Fig. 8). These features are noticeable in the statistical reconstructions based on sea surface height from 1993 to 2011 (Dong et al.

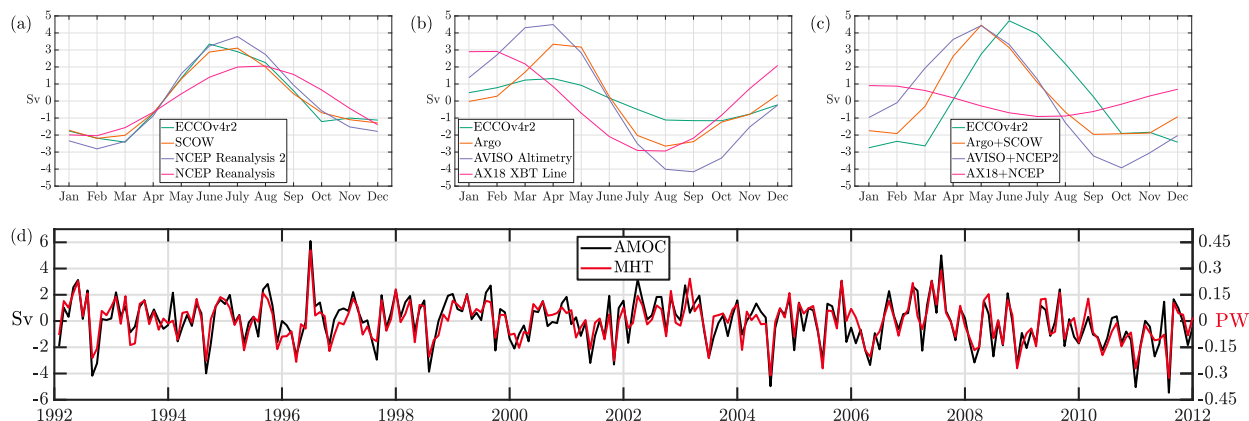


FIG. 1. (a)–(c) The seasonal cycle and (d) interannual anomaly for the SAMOC at 34°S . The time-mean value is removed from all to show variability. (a) The Ekman component of the SAMOC derived from the ECCOv4r2 wind stress fields (green), SCOW (Risien and Chelton 2008; orange), NCEP-2 (purple), and NCEP–NCAR reanalysis (pink). (b) The geostrophic component of the SAMOC computed from ECCOv4r2 density fields (green), Argo data (Dong et al. 2014; orange), satellite-altimetry-based sea surface height anomalies from AVISO (Duquet et al. 2000) based on the statistical relationship to temperature in Dong et al. (2015; purple), and from the first 17 transects of the trans-basin expendable bathythermograph (XBT) high-density line at 35°S (AX18) (Dong et al. 2009; pink). Geostrophic transport from ECCOv4r2 is computed with density fields via the thermal wind relation, using velocity fields at a reference depth of 1000 m to mimic the strategy used for the Argo data. (c) The total seasonal cycle in the SAMOC computed from ECCOv4r2 Eulerian velocity fields (green), the Argo geostrophic and SCOW Ekman components as in Dong et al. (2014; orange), the AVISO geostrophic reconstruction and NCEP-2 Ekman components as in Dong et al. (2015; purple), and the AX18 XBT geostrophic and NCEP Ekman components as in Dong et al. (2009; pink). All SAMOC estimates from observations and proxies were provided by S. Dong (2018, personal communication). (d) Interannual fluctuations of the SAMOC at 34°S (black) and MHT at 34°S (red) from 1992 to 2011, presented as monthly values with the seasonal cycle removed.

2015) and sea surface temperature from 1870 to 2015 (Lopez et al. 2017).

d. Adjoint model and linearized sensitivity calculation

We define our quantity of interest (QoI) δJ^m as

$$\delta J^m = J^m - J_0, \quad (3)$$

where J^m is the monthly mean SAMOC as in Eq. (2) during the m th month of 2011 (the last simulated year), and J_0 is the time mean over 1992–2011, so that δJ^m contains seasonal variability. We use the generic algorithm described in Forget et al. (2015a) to compute the sensitivity of SAMOC variability to external forcing $\partial J^m / \partial F_k$ linearized about the ECCOv4r2 state estimate. Here, $m = 1, 2, \dots, 12$ indexes the month in which the SAMOC is evaluated, and $k = 1, 2, \dots, 8$ indexes the surface atmospheric state variables listed in section 2a. We compute $\partial J^m / \partial F_k$ only from the SAMOC in 2011 so that the time window of integration in Eq. (5) is as long as possible, ensuring that the reconstructions in section 6 represent as much of the accumulated response to interannual atmospheric variability as possible. Additionally, we compute sensitivities of the SAMOC evaluated in each month of 2011 (i.e., 12 spatiotemporally varying sensitivities for each forcing variable) in order to get an accurate representation of seasonal variability. The adjoint code is derived with the commercial algorithmic

differentiation software Transformations of Algorithms in FORTRAN (TAF; Giering et al. 2005); computational details of this procedure in relation to the MITgcm are described in Heimbach et al. (2005).

3. SAMOC sensitivity pathways

The evolution of sensitivity patterns over time shed light on the dominant ocean dynamics carrying perturbations in each of the eight forcing variables to 34°S . Because we are interested in how a perturbation in external forcing affects the variability in the SAMOC at a later time, we discuss the sensitivities in reverse chronological order. Therefore, we define the lead or “memory” time τ_{mem} prior to t_f , the time when the objective function is evaluated (e.g., $\tau_{\text{mem}} = 1$ month corresponds to $t = t_f - 1$ month).

For a compact discussion on the important regions where atmosphere–ocean exchanges impact the SAMOC, we consider sensitivity maps from both wind stress components and the net heat and freshwater fluxes rather than each atmospheric state variable separately. The buoyancy fluxes are computed based on the atmospheric state variables (Large and Yeager 2004) and, in the context of sensitivities, provide a representative view of the physical mechanisms that carry atmospheric perturbations to 34°S . In particular, we show heat flux sensitivities in place of radiation, air temperature, and humidity sensitivities because they show the same qualitative picture and we can draw the same conclusions. Similarly, freshwater flux

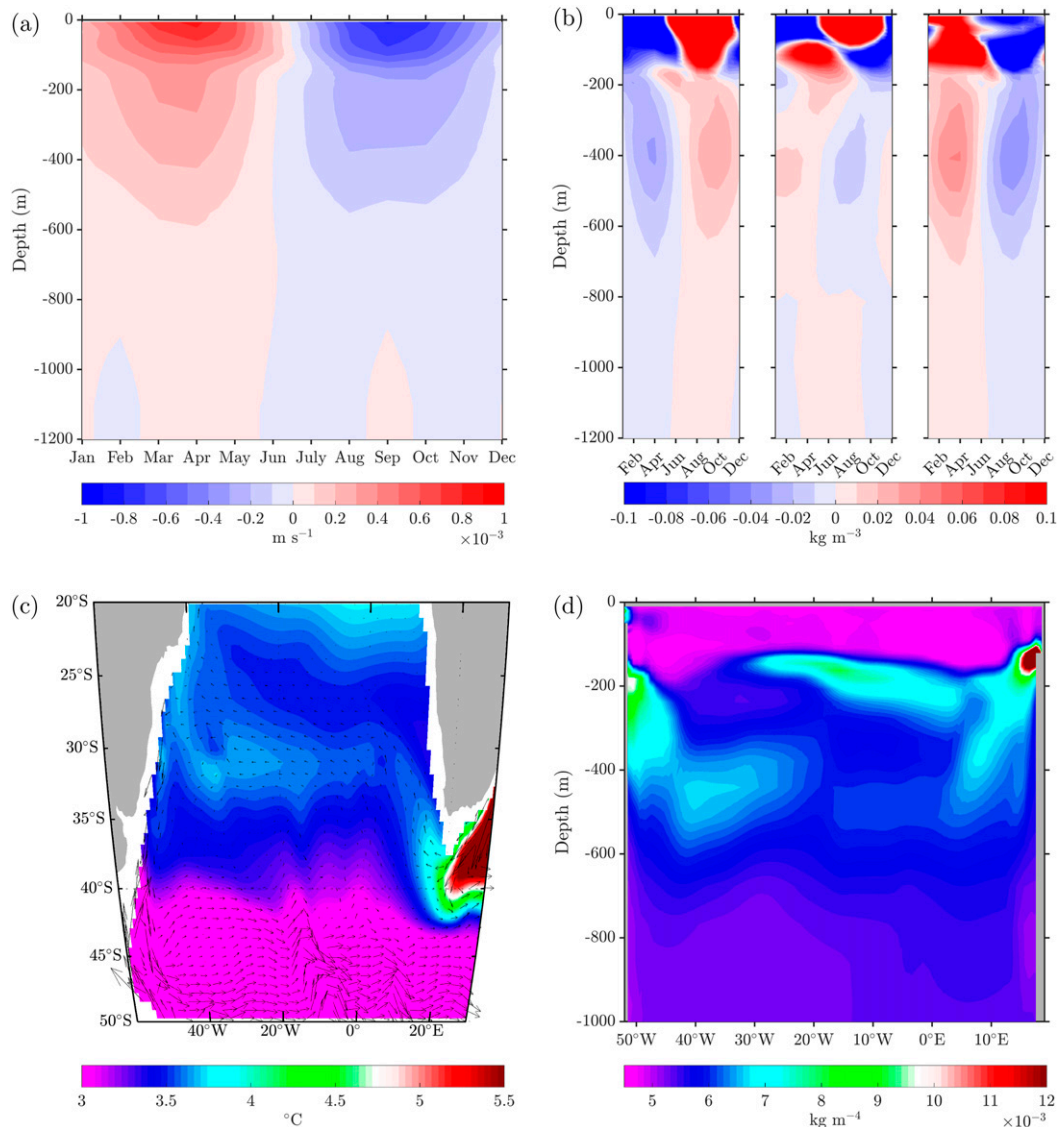


FIG. 2. Reproduction of geostrophic velocity, density, and temperature fields as in Dong et al. (2014) with ECCOV4r2 fields. The color maps have been chosen to match for direct comparison. (a) Seasonal cycle of the geostrophic meridional velocity fields derived from the thermal wind relation, using ECCOV4r2 density fields and meridional velocity fields interpolated between grid cells to 1000 m depth, which is used as the reference level. The time mean from each point has been removed to highlight variability. Compare to Dong et al. (2014, Fig. 2 therein). (b) Seasonal cycle of density at the (left) western and (middle) eastern boundaries, and (right) the difference between the two $\rho_e - \rho_w$. The western and eastern boundaries at 34°S are taken at 50.5°W and 16.5°E, respectively. The time mean is removed from each point to show variability. Compare to Dong et al. (2014, Fig. 3 therein). (c) The 1992–2011 time mean of potential temperature (color) and velocity field (vectors), interpolated between grid cells to 1000 m depth. Compare to Dong et al. (2014, Fig. 4a therein). (d) September vertical density gradient $-\partial\rho/\partial z$. Compare to Dong et al. (2014, Fig. 4d therein).

sensitivities show a similar picture as precipitation and continental runoff sensitivities.

In computing the sensitivities, we found that the sensitivity of the SAMOC with respect to wind stress is insensitive to the month for which the SAMOC is evaluated, while seasonality is important for variables affecting the buoyancy fluxes. That is, buoyancy forcing sensitivities

$\partial J^m / \partial F_k$ are slightly different depending on m , the month when the SAMOC is evaluated, while for wind stress, these gradients are independent of m . However, the differences in the buoyancy sensitivities are not readily discernible from visual inspection and are only important for the quantitative reconstruction of variability in sections 4–6. Therefore, we use sensitivities from a

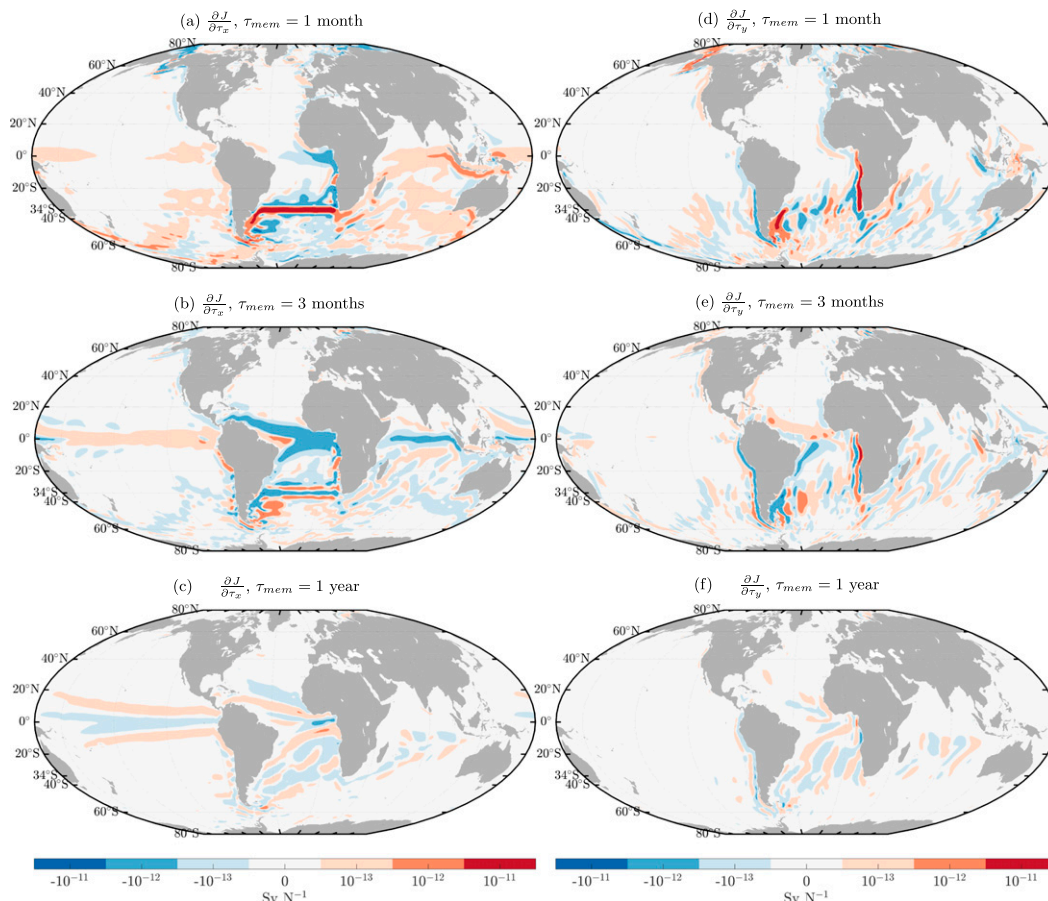


FIG. 3. Sensitivity of the SAMOC at 34°S to atmospheric momentum fluxes $\partial J/\partial F$ normalized by area in December. The forcing component in each column is (a)–(c) zonal wind stress and (d)–(f) meridional wind stress. Sign convention is such that an increase in (a)–(c) eastward wind and (d)–(f) northward wind over regions of positive sensitivity at a lead time given by τ_{mem} would increase the SAMOC at 34°S at final time. While these maps are relevant to the December SAMOC, the seasonal dependence is not readily discernable, and therefore this figure provides an informative representation of the important pathways and time scales for carrying perturbations to 34°S.

December-evaluated SAMOC in the following discussion of sensitivity patterns.

a. Sensitivity to wind stress

In this first month of lead time, the impact of local zonal wind stress is evident in the thick, positive band of sensitivity from 32°–36°S (Fig. 3a). The average sensitivity per grid cell between these latitudes is $0.16 \text{ Sv} (\text{N m}^{-2})^{-1}$, such that an increase in the westerlies over this region, $\delta\tau_x = 0.01 \text{ N m}^{-2}$, would increase northward transport at 34°S by 0.58 Sv over the next month. This value corresponds with Ekman theory to first order:

$$V_{\text{Ek}} = -\frac{\tau_x}{\rho_0 f}, \quad (4)$$

that is, a northward transport in the Southern Hemisphere is generated by a westerly wind stress. Indeed, assuming a reference density of $\rho_0 = 1030 \text{ kg m}^{-3}$ and

Coriolis parameter, $f = -8.13 \times 10^{-5} \text{ s}^{-1}$, theory would predict a northward transport of 0.79 Sv across 34°S resulting from the same perturbation. The disagreement between these arises from the fact that there are more processes averaged into the sensitivities within this region, while Ekman transport is the leading-order effect.

Previous studies (e.g., Köhl 2005; Heimbach et al. 2011; Pillar et al. 2016) have elucidated the interpretation of adjoint sensitivity patterns in terms of time-reversed, adjoint (or dual) Kelvin and Rossby waves that underlie basin-scale barotropic and baroclinic adjustment processes (Johnson and Marshall 2002a, 2004). As in these studies, our focus here is mainly on mechanisms governed by baroclinic processes. Nevertheless, the 1-month lead sensitivities in Figs. 3a and 3d still contain residuals of dual barotropic waves with global-scale signatures and merit brief discussion here. In particular, wind sensitivity patterns cover the South Atlantic, Indian, and, to a

lesser extent, Pacific Ocean basins. Past adjoint modeling experiments have shown 1-month lead sensitivities of the AMOC in the North Atlantic to be confined mostly within the basin, with some sensitivities in the South Atlantic [Pillar et al. (2016) show sensitivity at 25°N to momentum and buoyancy forcing, Bugnion et al. (2006) at 24°N to wind stress, and Heimbach et al. (2011) at 26°N to SSTs]. Here, we see a vastly different response, where the sensitivities show a discernible connection between the South Atlantic and neighboring ocean basins through linear wave dynamics.

Analyzing the structure of the 1-month sensitivity patterns in more detail reveals complex patterns that are set by basin geometry, latitude-dependent wave dynamics, and bottom topography, in particular in the Southern and Indian Ocean basins. The sensitivities along the South American, African, Indonesian, and Australian continental borders indicate that perturbations here are communicated to the SAMOC via barotropic coastally trapped waves. The pattern of alternating signs around topographic boundaries (e.g., the Mid-Atlantic Ridge in the Atlantic or the islands south of Madagascar) is due to topographic steering, where a barotropic wave must travel along f/H contours to conserve potential vorticity [see Pillar (2013) section 3.4.1 therein for details]. Additionally, midocean ridges are clearly seen as topographic boundaries for (dual) barotropic wave propagation, for example, the southern portion of the eastern Pacific rise and Southwest Indian Ridge. These bathymetric features limit barotropic wave propagation through the Indian Ocean basin, as shown by Matano et al. (1999, 2002). However, the more important pathway to the SAMOC is via Kelvin wave propagation through the Indonesian Throughflow, across the equatorial waveguide in the Pacific, and around the South American continent. This pathway connects the SAMOC to wind stress variability even on subseasonal time scales, as indicated in Fig. 3a. The subtleties of this teleconnection and verification of the sensitivity patterns here are highlighted in a forward perturbation experiment, which is described in the online supplemental material.

At lead times of two to three months, the broad patterns along the equator show that baroclinic equatorial Kelvin waves are important for communicating perturbations to the South Atlantic (Fig. 3b). These patterns remain significant even at lead times of one year in the Pacific, indicating a longer memory to perturbations in this basin than over the Indian Ocean. Beyond lead times of three months, dual baroclinic Rossby waves are discernable, indicating the time scale at which these wave dynamics propagate perturbations to the SAMOC (Figs. 3c,f). These signals are evident because of their northeast–southwest tilt, corresponding to the wave speed that is proportional to $\beta = \partial f / \partial y$.

After the barotropic and initial baroclinic response, wind stress sensitivities decay rapidly in magnitude. The RMS of global sensitivities drops by roughly an order of magnitude after one year of lead time, indicating that momentum flux perturbations beyond this time scale are relatively unimportant to the AMOC at 34°S. Throughout the 20 years of forcing lead time, wind stress sensitivities remain relatively negligible in the Northern Hemisphere, except at low latitudes, where the SAMOC is sensitive to the excitation of Rossby waves. This invariance to perturbations in the Northern Hemisphere corroborates the “equatorial buffer” theory developed by Johnson and Marshall, where the equator acts as a low-pass filter that dampens the effect of high-latitude forcing originating in the opposite hemisphere (Johnson and Marshall 2002a, 2004).

b. Sensitivity to freshwater forcing

Precipitation and continental runoff perturbations have a direct impact on sea surface height, thus the sensitivity pattern due to a rapid barotropic adjustment covers the globe one month prior to AMOC evaluation (Fig. 4a). At a lead time beyond one month, most variability is communicated to the SAMOC via Rossby waves and advection through the Antarctic Circumpolar Current (ACC). At just over one year of lead time, the sensitivity patterns in Fig. 4b show that the influence of freshwater forcing is advected along the ACC, through the Drake Passage, and up the South American coast to the SAMOC. A similar pattern is visible south of the Indian Ocean at a lead time of five years and south of the Australian continent three to four years prior to reaching the SAMOC. Semiannual to annual variability in the Malvinas Current has been investigated in the context of wind stress perturbations in the ACC (e.g., Fetter and Matano 2008). Here, sensitivity patterns show the relevant pathway for variability on similar time scales originating from air–sea buoyancy exchanges. In particular, this advective pathway communicates perturbations in freshwater forcing originating in the Indian Ocean basin through the ACC, resulting in a maximum amplitude of ~ 0.1 Sv of interannual variability in the SAMOC (Fig. 9c). While the magnitude of response is relatively small for the SAMOC, it shows the usefulness of the adjoint in exposing the complex dynamical link between the ACC, SAMOC, and potentially the Malvinas Confluence on time scales from six months to five years.

Barotropic and baroclinic Rossby waves dominate as the main pathway for communicating perturbations from the Indian Ocean. Along the east African coast, boundary waves are evident in the first year of lead time, transporting variability along the Mozambique Channel. Baroclinic Rossby waves are evident in the Indian Ocean interior at

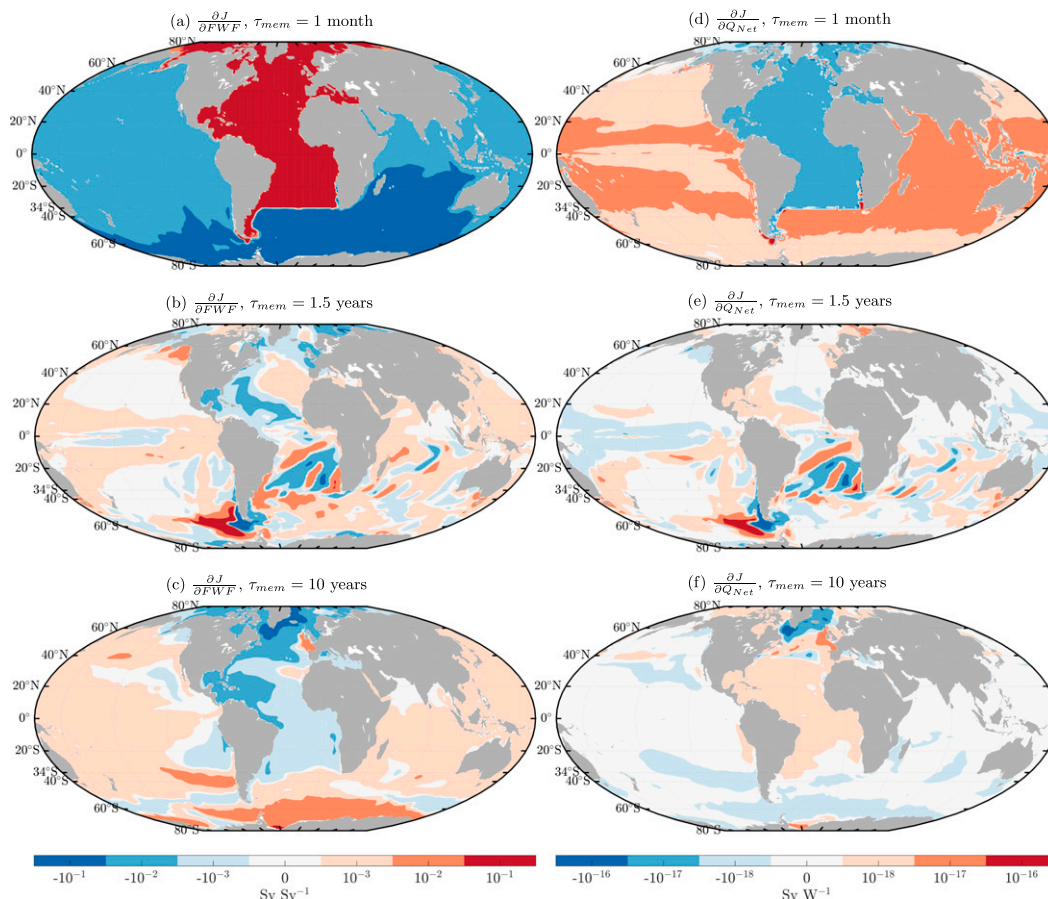


FIG. 4. As in Fig. 3, but for buoyancy fluxes: (a)–(c) freshwater flux and (d)–(f) heat flux. Sign convention is such that an increase in (a)–(c) freshwater input (e.g., precipitation) and (d)–(f) downward heat flux (i.e., ocean heating due to increased air temperature) over regions of positive sensitivity at a lead time given by τ_{mem} would increase the SAMOC at 34°S at final time.

1.5 years of lead time (Fig. 4b), although the amplitude is much smaller than in the South Atlantic.

In contrast to the wind stress patterns, freshwater forcing sensitivities decay slowly. At one year of lead time, the spatial RMS of the sensitivities is reduced by one-half and remains nearly constant beyond two years of lead time. After roughly 10 years of lead time, sensitivities in the North Atlantic subpolar gyre are the largest in magnitude (Fig. 4c). This behavior gives rise to low-frequency variability in the AMOC at 34°S, although at much smaller amplitude than any variability induced by wind stress (see section 6b).

c. Sensitivity to thermal forcing

In the first three years of lead time, thermal forcing sensitivities largely resemble the freshwater flux sensitivity patterns. For instance, the pattern highlighting the ACC as a pathway for advecting heat flux perturbations to 34°S is visible here (Fig. 4e). We also note that

sensitivities cover the entire globe in the first month as part of a fast barotropic response, similar to that shown by the precipitation component (cf. Figs. 4a and 4d). This response is permitted through the air–sea flux formulation from Large and Yeager (2004), where evaporation is computed from the prescribed precipitation and thermal forcing fields. This computation links changes in the net heat flux to sea surface height, allowing for rapid adjustment in the SAMOC from thermal forcing perturbations. We note that this response is not exhibited in Pillar et al. (2016, see Fig. 1g therein), and this is simply due to model setup: They prescribe the heat flux, whereas we compute it here based on the surface atmospheric state.

Beyond lead times of roughly four to five years, the patterns reflect seasonal changes in mixed layer depth. The strongest remaining signal is in the North Atlantic subpolar gyre during boreal winter months when the mixed layer is deeper (Fig. 4f), reflecting deep convection.

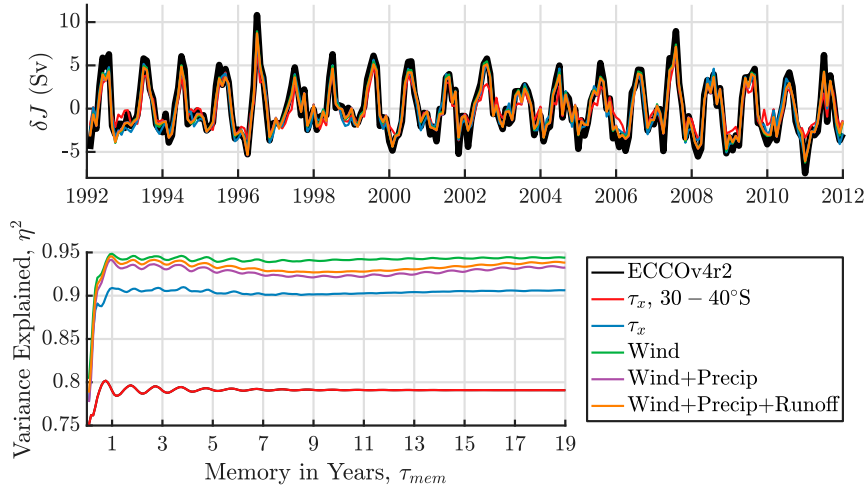


FIG. 5. (top) AMOC at 34°S computed from the forward model (black line) and reconstructions as in Eq. (5), where each colored line denotes the included external forcing in the integral. Lead time for each reconstruction is 19 years. (bottom) Variance explained computed via Eq. (6). Wind reconstruction contains global contributions from both τ_x and τ_y .

Because the adjoint model cannot accurately represent this process beyond a few years, the sensitivities are artificially high. These errors are discussed further in section 6c.

4. Reconstruction of the 20-yr SAMOC

We use the sensitivities discussed in section 3 to reconstruct monthly SAMOC variability from 1992 to 2011 [Eq. (3)]. Assuming that the sensitivities are stationary with respect to the month in which the AMOC is evaluated and the dependence of the monthly AMOC varies linearly with external forcing, we can reconstruct the signal via the convolution integral:

$$\begin{aligned} \delta J_{\text{Rec}}(t) &= \sum_k \delta J_k(t) \\ &= \sum_k \int_{t-\tau_{\text{mem}}}^t \int_X \int_Y \frac{\partial J^m}{\partial F_k}(x, y, t-s) \delta F_k(x, y, s) dx dy ds. \end{aligned} \quad (5)$$

Here, s is the dummy variable for integration in time and τ_{mem} denotes the memory or lead time of the objective function. The longest lead time available is 19 years, corresponding to the simulated time window. Note that the QoI δJ^m is diagnosed from the forward model during the m th month of 2011 for computing sensitivities and is separate from the reconstruction $\delta J_{\text{Rec}}(t)$, which is computed for each month from 1992 to 2011. The month m associated with the sensitivity $\partial J^m / \partial F_k$ is equal to the month of the reconstruction $\delta J_{\text{Rec}}(t)$. For example, to reconstruct the variability for each January month, we compute $\delta J_{\text{Rec}}(t)$

for $t = (t_1, t_{13}, t_{25}, \dots)$ using sensitivity maps computed from the SAMOC evaluated in January 2011: $\partial J^1 / \partial F_k$.

The reconstructed SAMOC at 34°S accounts for the accumulation of forcing perturbations up to a 19-yr lead time (Fig. 5, top). We have neglected the contribution from air temperature, radiation, and humidity because these components cause a divergence in the reconstruction (see section 6c for a discussion). Despite these limitations, the reconstructed monthly mean SAMOC $\delta J_{\text{Rec}}(t)$ is remarkably consistent with the forward model output $\delta J_{\text{Fwd}}(t)$. Although we have no depiction of posterior uncertainty arising from model error for either quantity, the reconstructed SAMOC reproduces nearly all of the variability captured by the forward model. This agreement is depicted by variance explained, which we compute as

$$\eta^2(\tau_{\text{mem}}) = 1 - \frac{\text{var}[\delta J_{\text{Fwd}}(t, \tau_{\text{mem}}) - \delta J_{\text{Rec}}(t, \tau_{\text{mem}})]}{\text{var}[\delta J_{\text{Fwd}}(t, \tau_{\text{mem}})]}. \quad (6)$$

This metric is shown for various reconstructions in Fig. 5 (bottom) as a function of lead time, where each colored curve is generated by restricting the integral in Eq. (5) to various forcing components. The red curve is further restricted to only account for zonal wind stress perturbations in the region 30°–40°S to highlight the large contribution of variability originating from local forcing perturbations. Clearly, wind stress perturbations drive the majority of the variability in the forward model, where local zonal wind stress is the largest single contributor to the modeled SAMOC variability. In the following sections, we discuss the seasonal and interannual variations in the SAMOC, showing the geographical

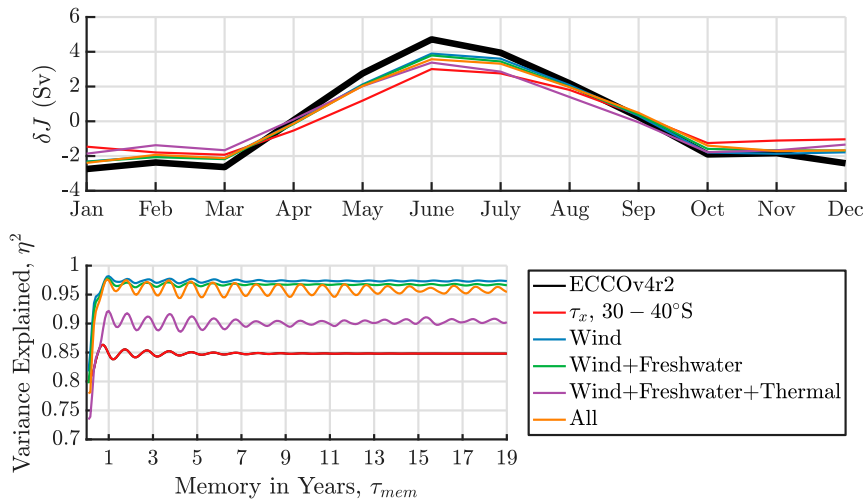


FIG. 6. (top) Reconstructed SAMOC seasonal cycle computed as 1992–2011 climatologies of curves in Fig. 5, with the time mean removed. Annual averages are removed before computing the climatologies to eliminate interannual trends. Lead time for each reconstruction is 19 years. (bottom) Variance explained of seasonal cycle. Contributions from precipitation and continental runoff are included in “freshwater,” air temperature and radiation are included in thermal, and humidity is additionally included in all.

distribution of atmospheric forcing that contributes to this variability.

5. Attribution of seasonal variability

The seasonal cycle in the AMOC at 34°S is shown in Fig. 6, diagnosed from ECCOv4r2 and reconstructed from various forcing components. Here, annual averages have been removed before computing the climatology to eliminate any interannual trends. In Fig. 6, contributions from air temperature and radiation (denoted by “thermal”) as well as humidity (included in “all”) are included because the reconstructed seasonal cycle with these variables included does not diverge from the forward model.

The seasonal cycle is well approximated even with a short memory because wind stress, which acts on short time scales (e.g., Pillar et al. 2016), is the dominant variable in reconstructing this signal. Figure 6 highlights the crucial role of fast, wind-driven adjustments in establishing the seasonal cycle in the SAMOC. When only three months of historic wind forcing are accounted for, 90% of the seasonal SAMOC variability is recovered. This value converges quickly after one year to ~97%.

a. Seasonal attribution to wind stress

The reconstructions of the SAMOC seasonal cycle originating from global wind stress perturbations, that is, δJ_{τ_x} and δJ_{τ_y} in Eq. (5), are shown in Figs. 7a and 7b, respectively, as the accumulated response to 19 years of

forcing. Here, the bars denote the magnitude of contribution to δJ_{τ_x} and δJ_{τ_y} from various regions, computed by restricting the spatial domain of integration in Eq. (5). In the figure, the regions that provide the largest total magnitude of SAMOC variability across all months are shown and the net impact from the rest of the globe is condensed to “other.”

Locally generated ($\pm 5^\circ$) wind stress perturbations account for the greatest single component of the SAMOC’s seasonal cycle, accounting for 85% of the variance explained (Fig. 6). Even at a lead time of one month, this locally generated variability corresponds to $\eta^2 = 80\%$. On these time scales, this portion reflects perturbations resulting mostly from Ekman transport due to seasonal fluctuations in the local westerlies.

Wind stress fluctuations over the tropical Atlantic generate a seasonal cycle of roughly 2 Sv and provide the second largest contribution to the SAMOC climatology. To leading order, most other contributions are generated in the Indian Ocean. To quantify the time scale at which variability is communicated from these regions, we consider the quantity:

$$\varepsilon(\tau_{mem}) = \sum_{t=t_0}^{t_f} \frac{|\delta J_{Rec}(t, \tau_{mem}) - \delta J_{Rec}(t, \tau_{mem} = 19 \text{ years})|}{|\delta J_{Rec}(t, \tau_{mem} = 19 \text{ years})|}, \quad (7)$$

where the summation over $t \in [t_0, t_f]$ is carried out over the model simulation time, that is, 1992–2011. Thus, for a given region and forcing component, $\varepsilon(\tau_{mem})$ gives

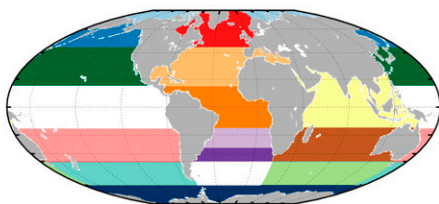
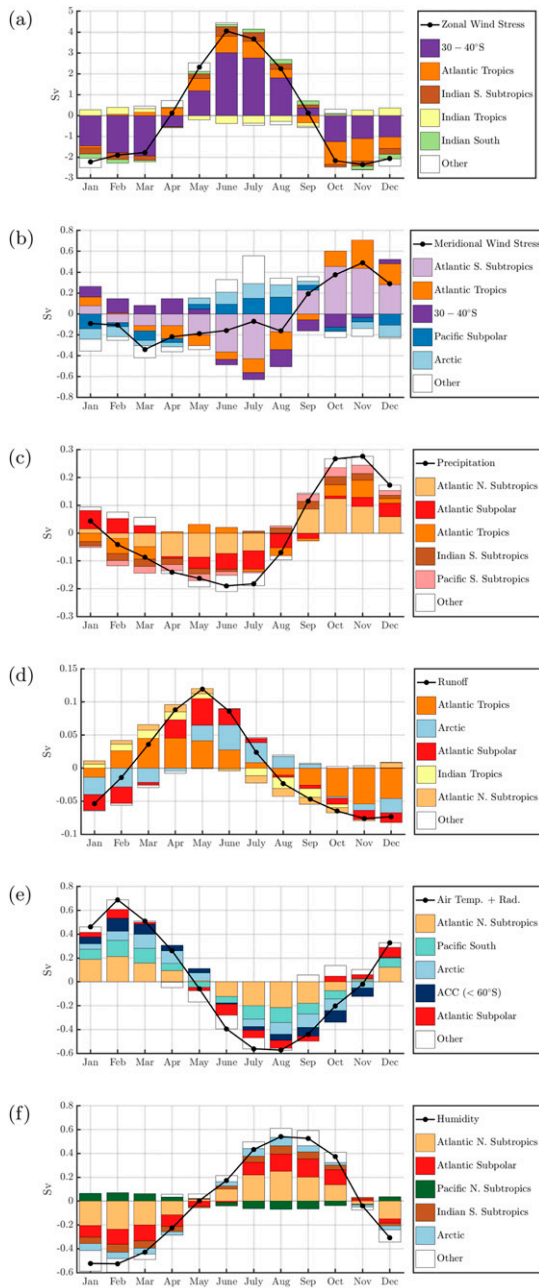


FIG. 7. Seasonal cycle originating from perturbations in each external forcing variable, with the time mean removed. The black line depicts the reconstruction when global contributions are included. The colored bars denote the magnitude of contributions arising from that forcing component over a region of the globe.

an indication of how the reconstruction improves with lead time. The signals from the tropical Atlantic and Indian Ocean basins are communicated quickly as ϵ for each region drops below 5% after only three months, corresponding to the approximate time scales for first-mode baroclinic Kelvin waves to communicate perturbations from the tropics and Indian Ocean to 34°S. From 6 to 12 months, the amplitude of variability from these regions increases slightly due to an accumulation of perturbations communicated by slower-traveling baroclinic Rossby waves originating from the South Atlantic.

In general, zonal wind stress generates variability that is roughly an order of magnitude larger than that of the meridional component on seasonal time scales. The magnitude of each signal is governed by the strength of perturbations from each component and how well the perturbations project onto the sensitivity patterns shown in Fig. 3. Clearly, zonal wind stress perturbations are much stronger than those in the meridional direction. Additionally, the sensitivity patterns for zonal wind stress are much broader, and forcing projects strongly onto these patterns. For example, westerly perturbations around 30°–40°S project strongly onto the thick band of sensitivity here, driving Ekman transport. On the other hand, the dominant patterns relevant to meridional wind stress are in the upstream coastal waveguides (Fig. 3d) along the African coast north of 34°S and along the South American coast south of 34°S. Along the African coast, for example, northward (southward) perturbations generate offshore (onshore) Ekman transport, resulting in a zonal pressure gradient that drives northward (southward) geostrophic transport. However, because the seasonal forcing over these regions is overall weak, their impact is balanced by forcing from remote regions and the total contribution to the SAMOC climatology is relatively small.

b. Seasonal attribution to freshwater forcing

Freshwater flux perturbations generate variability at much smaller amplitudes than wind stress because there is a spatial mismatch between forcing and sensitivities from 1992 to 2011, consistent with Pillar et al. (2016). After the fast barotropic response, the largest sensitivities

(a)–(f) The top five regions that contributed the greatest magnitude to the SAMOC seasonal cycle and collapse all others into the “other” bar. Note the difference in scale for each y axis. Lead time in each reconstruction is 19 years. (Note that there is usually some degree of cancellation between regional reconstructions, hence some stacked bar values exceed and are of opposite sign of the value for δJ_{Rec} in a given month.)

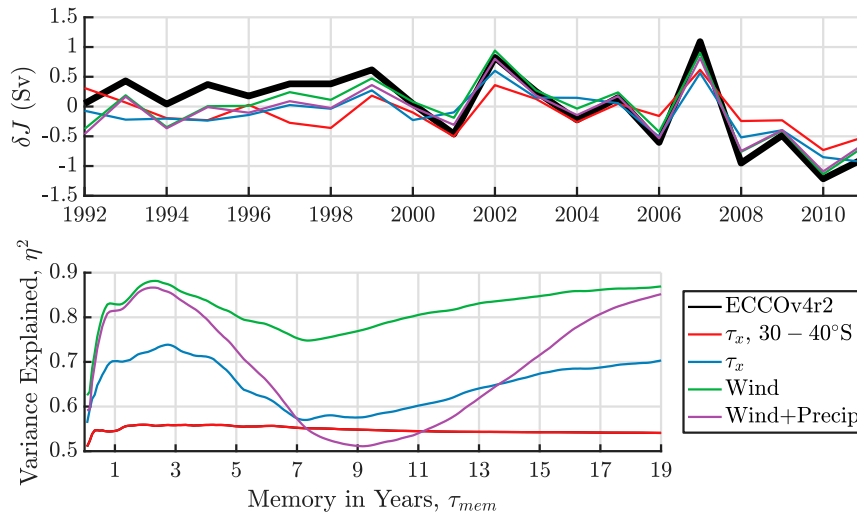


FIG. 8. (top) Reconstructed SAMOC interannual variability from 1992 to 2011, computed as annual averages of curves in Fig. 5, with the time mean removed. Lead time for each reconstruction is 19 years. (bottom) Variance explained as in Eq. (6).

are concentrated across the North Atlantic and Southern Ocean basins, with a relatively weaker signal across the equator and in the tropics. By contrast, the strongest freshwater forcing originates from precipitation near the intertropical convergence zone and runoff at the mouth of the Amazon River. The mismatch between sensitivities and forcing patterns is evident in the quantity ε [Eq. (7)], which drops below 5% with only one month of lead time for these forcing components. Thus, the widespread barotropic response (Fig. 4a) is a key mechanism for communicating freshwater perturbations to 34°S. We additionally note that the reconstructed seasonal cycle from precipitation and runoff are out of phase with one another (Figs. 7c,d) so that the net contribution to the SAMOC climatology is minimal.

c. Seasonal attribution to thermal forcing

Radiative and air temperature (or to first-order sensible heat flux) variability generates signals that are largely in phase with one another, and the most important contributions come from similar regions. Thus, the resulting seasonal SAMOC from each of these fluxes is shown in Fig. 7e to provide a concise description of their impact. Thermal forcing from these components projects strongest onto the geostrophic component of SAMOC transport, as the resulting curve shown in Fig. 7e is nearly in phase with the geostrophic component in Fig. 1b. SAMOC variability originating from these fields takes longer to accumulate than that from the precipitation and wind stress components. Here, it takes roughly two years for ε to drop below 5% because variability originating from these components is due

to the accumulation of slower-traveling baroclinic Rossby waves and advection in the ACC (Fig. 4e).

The seasonal cycle generated by humidity perturbations, impacting the SAMOC through the latent heat flux, is shown in Fig. 7f. The phase is almost exactly opposite such that altogether the net heat flux contributes a negligible impact on the overall seasonal cycle (~ 0.1 Sv). In total, buoyancy forcing generates a seasonal cycle in the SAMOC with a maximum amplitude of 0.4 Sv, and is largely generated by perturbations in the North Atlantic subtropical and subpolar gyres, and the Southern Ocean communicated via advection in the ACC.

6. Attribution of interannual variability

Interannual variability in the SAMOC is shown in Fig. 8, which presents annual averages of the reconstructions in Fig. 5. We do not include the interannual response attributed to continental runoff because this forcing is represented as a climatology in the model, generating less than ± 0.01 Sv of interannual variability. We also exclude the contributions from radiation, air temperature, and humidity because linear approximations in the adjoint model cause these reconstructions to diverge. We discuss this issue in section 6c.

Most of the interannual variability is captured with lead times of roughly two years, but beyond this point, η^2 [Eq. (6)] does not behave monotonically with memory. In particular, the reconstruction that includes precipitation and wind stress forcing shows degradation with increasing memory from two to nine years (Fig. 8). This behavior corresponds to the resolution of roughly

decadal variability originating from the North Atlantic subpolar gyre. We also note that even when accounting for precipitation and wind stress perturbations, η^2 never reaches the value attained by the wind-forced reconstruction. This gap between the reconstructions is likely due to the small time window for resolving the decadal variability discussed in section 6c. The mismatch could also be due to the lack of thermal variables in the reconstruction, which could be important for fully resolving contributions from buoyancy forcing, assuming they are well represented.

a. Interannual attribution to wind stress

The regional attribution of interannual SAMOC variability from wind stress perturbations is shown in Figs. 9a and 9b, as the accumulated response to 19 years of forcing. The importance of wind stress in reconstructing interannual variability corroborates results from forward perturbation experiments by Yeager and Danabasoglu (2014), where momentum fluxes are shown to dominate the AMOC on these time scales south of the equator. Maximum fluctuations are roughly 1 Sv, and again wind stress over 30°–40°S in the South Atlantic provides the largest magnitude of variability in the annually averaged SAMOC (Fig. 9a). However, while the contribution from this region is a major component in the annual fluctuations, particularly for zonal winds, perturbations here do not dominate interannual SAMOC variability as with the seasonal cycle (cf. Fig. 6). Instead, wind stress perturbations from remote locations balance the contribution from relatively local regions.

Wind stress over the tropical Pacific provides the second largest impact on interannual SAMOC variability (Fig. 9a). It takes roughly 13 years for ε [Eq. (7)] to drop below 5% for this region. This time scale and the broad wave patterns that remain important at lead times greater than a year (Fig. 3c) indicate that slow baroclinic Rossby waves are crucial for communicating perturbations that drive this transport variability at 34°S.

Over the South Atlantic and Pacific sectors of the Southern Ocean (40°–60°S), wind stress has a notable impact on interannual SAMOC variability (Figs. 9a,b). Forcing over these regions generates a maximum magnitude of roughly 0.25 Sv in the annual SAMOC, which is similar to forward perturbation results shown by Yeager and Danabasoglu (2014, see Fig. 13d therein). Here, it is important to note that eddies, when resolved or permitted, can compensate the impact of Southern Hemisphere westerlies on the AMOC (Farneti and Delworth 2010). To incorporate this effect, coarse-resolution models must employ an eddy parameterization with a Gent and McWilliams (1990) (GM) coefficient as a 3D field dependent on the ocean state and its response to the winds

(Gent and Danabasoglu 2011). The ECCOv4r2 framework allows for a similar flow of information from the ocean state to the mixing parameter values at each grid cell through the model adjoint. We additionally take a degree of confidence in the ECCO solution as it has been shown that the resulting mixing parameters allow for a vastly improved fit to observations (Forget et al. 2015b). Of course, an in depth analysis of the differences between mixing parameters derived in ECCOv4r2 and those from prognostic schemes, for example, as implemented in Gent and Danabasoglu (2011), would be interesting future work.

While zonal wind stress is clearly the dominant forcing component for driving interannual variability in the SAMOC at 34°S, the meridional component is significant, explaining roughly 15% of the variance (Fig. 8). Trapped boundary waves in the upstream waveguides along the Argentinian and West African coast in the Atlantic, as well as along the Chilean coast in the Pacific (Fig. 3d) are responsible for communicating the greatest impact.

b. Interannual attribution to precipitation

On interannual time scales, freshwater forcing generates variability that is smaller but comparable in magnitude to that generated by wind stress. The contribution from various regions across the globe is shown in Fig. 9c. In contrast to wind forcing, surface freshwater forcing drives SAMOC variability on decadal time scales, which is only partially resolved over the time series in this study. These fluctuations are permitted by relatively time-invariant sensitivity patterns at lead times greater than 10 years that decay slowly in amplitude, indicating that the SAMOC has a long memory to freshwater adjustments.

The strongest response in the annual SAMOC from precipitation is generated by forcing over the North Atlantic subpolar gyre, which is the region with the largest amplitude sensitivity patterns (Fig. 4c). Here, the weakening SAMOC over the 1990s is generated by positive perturbations in precipitation in the 1980s to early 1990s that project onto the strong, negative sensitivity pattern here. Negative precipitation forcing in the early 2000s then generates a strengthening SAMOC into 2011. We note that this regional trend in the interannual precipitation field is about an order of magnitude smaller than the seasonal cycle but is present in both the ECCO-adjusted precipitation field and that from the Global Precipitation Climatology Project (GPCP; Huffman et al. 1997). It is much weaker in the ERA-Interim dataset without ECCO adjustments (Dee et al. 2011). However, no matter which dataset is used, the “bell shaped” curve in the SAMOC reconstruction from precipitation forcing over this region is still present, with amplitude

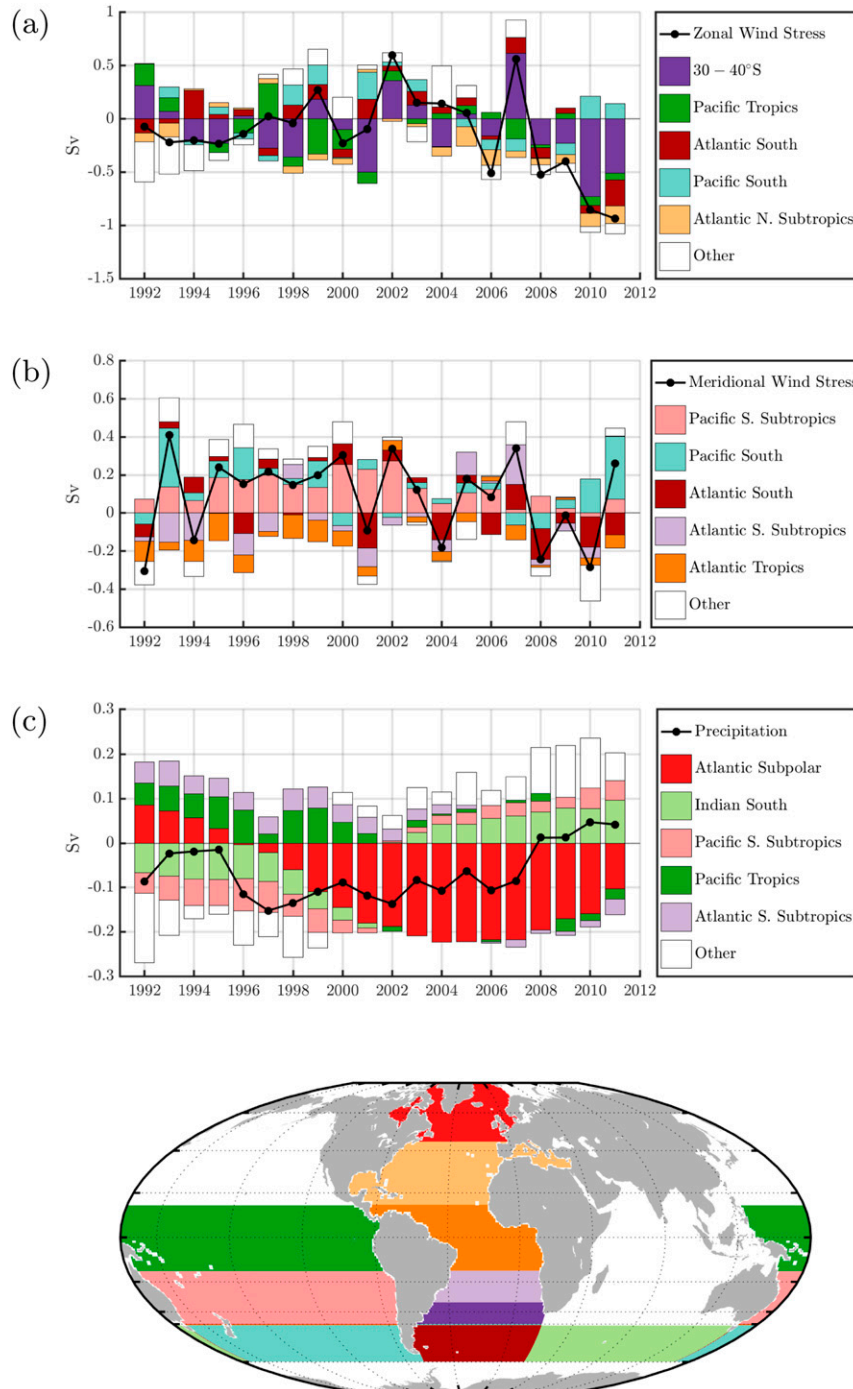


FIG. 9. As in Fig. 7, but showing the regional contributions for interannual variability. Again, note the difference in scale for each y axis. Lead time is again 19 years.

0.1 Sv (GPCP, ERA without adjustments; not shown) to 0.2 Sv (ECCOv4r2 forcing; shown in Fig. 9c). Additionally, this roughly decadal pattern in the SAMOC from precipitation over the North Atlantic subpolar gyre is comparable to what is shown by forward

sensitivity experiments in Yeager and Danabasoglu (2014, see Fig. 12d therein), where the authors isolate AMOC variability resulting from interannual freshwater flux perturbations over the Labrador Sea. A similar response is also noticeable at a different phase in the

AMOC at 25°N (Pillar et al. 2016, see Fig. 6f therein). However, the amplitude of the freshwater-forced variability in the SAMOC is roughly one-tenth of that in the Northern Hemisphere AMOC. The weaker signal in the South Atlantic can be explained by the equatorial buffer theory, which describes how the equator dampens the effect of high-latitude forcing originating in the opposite hemisphere (Johnson and Marshall 2002b).

c. Interannual attribution to thermal forcing

The interannual reconstructions for air temperature, radiation, and humidity cause the SAMOC reconstruction to diverge from the ECCOV4r2 forward model. The interannual reconstruction of SAMOC variability forced by shortwave radiation is shown as an example of this behavior in Fig. 10. Here, as the time integral in Eq. (5) is carried out over lead times beyond five years, the reconstructions show an increasing trend in the SAMOC that is not physically valid as these trends are not present in the ECCOV4r2 solution.

The reason for this unphysical behavior in the reconstruction is due to the inaccuracy of the adjoint model in representing the sensitivity to thermal forcing over regions where convection is important. First, there are artificially high sensitivities in the North Atlantic subpolar gyre because of the linearized adjoint model's inability to represent deep convection in this area. Second, in the Weddell Sea, sensitivities are unphysically high because of parameterization schemes of brine rejection from sea ice formation. Here, dense surface water filled with brine is simply pushed to a lower layer of the ocean, carrying surface heat fluxes with it. Representing these processes in the adjoint model is a challenge, and more work is necessary to determine if inaccuracies here are inherent to the linearization of these complex phenomena, or if they are simply caused by inadequacies in the computational model.

Omitting these highly sensitive regions in the SAMOC reconstructions from thermal forcing unsurprisingly results in negligible interannual fluctuations. The resulting pattern is similar to the reconstruction in Fig. 10 with one year of lead time but is centered around -0.4 Sv. However, because this behavior is also not exhibited in the forward model, we omit the contribution from these variables entirely in order to avoid interpreting results that may not be physically relevant.

7. Conclusions

We have used a numerical model that was fit to observation data from 1992 to 2011 via the ECCOV4r2 state estimation procedure (Forget et al. 2015a) to characterize and quantify in space and time the atmospheric origins

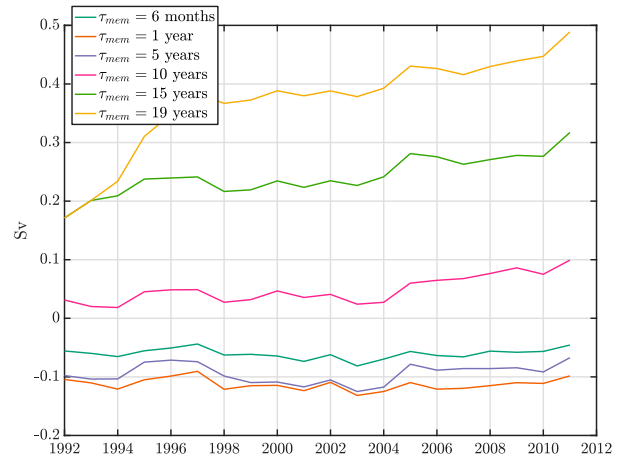


FIG. 10. Interannual SAMOC variability reconstructed purely with shortwave radiation. The time window for the integral in Eq. (5) is increased to show how the reconstruction diverges with increasing memory.

of variability in the AMOC at 34°S (referred to as SAMOC), which are communicated via ocean dynamics. Comprehensive spatial and time-lagged patterns of sensitivities computed from the adjoint model reveal the dynamical linkage between atmospheric forcing and the SAMOC. In contrast to what has been shown in the North Atlantic (e.g., Pillar et al. 2016), these patterns exhibit a widespread domain of influence on SAMOC variability, spanning across neighboring ocean basins even on short time scales. These maps highlight the importance of Kelvin, Rossby, and coastally trapped wave dynamics in translating remote atmospheric perturbations to time-lagged variability in the northward volume transport in the Atlantic.

The dynamical reconstruction of the SAMOC computed from these sensitivities captures the variability exhibited in the ECCOV4r2 forward model with remarkable accuracy and thus provides a skillful surrogate of the full nonlinear model. By segmenting the convolution integral used for reconstruction, we show the dominant atmospheric variables and regions of influence in governing seasonal to interannual fluctuations in the SAMOC. The majority of variability modeled by ECCOV4r2 on these time scales is attributed to perturbations in the zonal wind stress field, generating a seasonal cycle ranging from -2 to $+4$ Sv. Seasonal fluctuations are largely attributable to local perturbations over the latitudinal band 30°–40°S, driving Ekman transport with lead times up to one month. Meridional wind stress and buoyancy flux perturbations drive a seasonal cycle that is roughly an order of magnitude smaller in amplitude, at roughly 0.4 Sv each. Interannual variability, represented as annual averages, is smaller, with a maximum amplitude of 1 Sv. SAMOC

variability on these time scales is generated by a complex accumulation of forcing over remote regions of the world. Perturbations in the zonal wind field over the tropical Pacific, for instance, are shown to have a notable impact on the SAMOC at these time scales. While momentum fluxes still dominate, freshwater forcing has a more comparable impact due to low-frequency variability generated by forcing over the North Atlantic subpolar gyre.

The amplitude of the seasonal cycle induced by geostrophy at 34°S in the ECCOv4r2 model is relatively weak compared to estimates from Argo (Fig. 1b; Dong et al. 2014). Adding density profiles from mooring arrays as data constraints within the optimization framework could help to resolve the disagreement here and is an important area of future work for better constraining the modeled overturning circulation. An even closer fit to the Argo data would slightly modify the phase of the SAMOC seasonal cycle from ECCOv4r2. Nevertheless, we expect the sensitivity patterns shown here, which reveal the dynamical mechanisms in the ocean that communicate atmospheric perturbations to 34°S, to be robust.

The attribution of interannual variability to surface heat fluxes is omitted in this analysis because deep convection in the subpolar gyre and the parameterization of brine rejection in the Weddell Sea are not represented well by the linearized adjoint model. In particular, unphysically high sensitivities are generated in these regions such that the reconstructions with these variables diverge from the forward model solution. These variables are not expected to provide a large contribution to the interannual variability within the 20-yr time frame of this study, however, because momentum fluxes are shown here and previously (Yeager and Danabasoglu 2014) to be most important. A better understanding of the AMOC response to high-latitude heat fluxes is nevertheless important for inverse modeling and presents an important area of future work, particularly for regions where buoyancy-driven adjustments make a larger contribution to the total transport variability.

The model resolution in this study ($1^\circ \times 1^\circ$) presents a limitation of the analysis as the impact of eddies on the AMOC is fully parameterized. Eddies have been shown to play an important role on AMOC variability, for instance through the shedding of mesoscale eddies from the Agulhas leakage (Biaostoch et al. 2008) and the compensation of Southern Hemisphere westerly forcing (e.g., Farneti and Delworth 2010). While the ECCOv4r2 optimization gives a degree of confidence that the resulting mixing parameters sustain observed oceanic features (Forget et al. 2015b), it remains to be quantified how well the parameterizations capture eddy impacts on the large-scale circulation. Specifically, disentangling the contribution of these eddy processes on SAMOC

variability and the ability of the optimized parameters to represent their impact is clearly an important area of future work, for which the present study provides an important baseline.

We have shown that AMOC variability is the result of integrating perturbations that are generated from effectively independent processes in space and time, as was concluded in Wunsch and Heimbach (2013b). In particular, the dominant impact of wind forcing for skillful reconstruction of SAMOC variability has important implications on predictability, as it places stringent requirements on atmospheric predictability for forecasting seasonal to interannual SAMOC variations. Our findings highlight the challenge in attributing observed variability in the AMOC to their points of origin and the lack of a monocausal relationship between isolated forcings and the AMOC response. More generally, these challenges motivate the need for continued, widespread observation of the atmosphere and ocean in order to attribute or (eventually) forecast variability in the AMOC.

Acknowledgments. Supported in part through NASA via JPL/Caltech subcontract “ECCO: Understanding Sea Level, Ice, and Earth’s Climate” and through the NOAA grant NOAA/NA130AR4310135. T.S. acknowledges support through an ICES CSEM fellowship. We thank Gael Forget and An T. Nguyen for help with aspects of the model configuration (especially the model adjoint) and analysis tools. We also thank Carl Wunsch and Helen Pillar for a wealth of helpful comments that improved the manuscript. T.S. additionally thanks the NOAA scientists at the 2017 U.S. AMOC Science Team Meeting for helpful discussion and Shenfu Dong for correspondence regarding the SAMOC computed from observation data and proxies. We acknowledge useful comments from three anonymous reviewers that strengthened the manuscript.

APPENDIX

Extension of ECCO Forcing Fields to Cover the Period 1979–2011

The ECCOv4r2 atmospheric state fields extend from 1992 to 2011, including adjustments to ERA-Interim fields (Dee et al. 2011) from the optimization in Forget et al. (2015a). Using these fields alone means that the reconstruction of the first year (1992) of SAMOC variability will be relatively inaccurate because the convolution integral can only extend back to January 1992. Additionally, any low-frequency mode in the SAMOC will require a longer lead time in order to capture any low-frequency perturbations causing that variability. Thus, it is important to use forcing data that extend as

far into the past as possible while maintaining consistency with the ECCOv4r2 setup.

To provide longer lead times in the reconstruction, we prepend the ECCOv4r2 atmospheric state variable records with ERA-Interim fields from 1979 to 1991. Additionally, to capture time-mean features of the adjustments inferred from the optimization procedure, we added a climatology of the ECCOv4r2 adjustments to the ERA-Interim fields as follows:

$$F_k(x, y, t) = F_k^{\text{ERA}}(x, y, t) + \tilde{F}_k(x, y, m),$$

where k indexes the forcing variables, t indexes each month in 1979–91, m is the month associated with t , $F_k^{\text{ERA}}(x, y, t)$ gives the atmospheric state variable from Dee et al. (2011), and $\tilde{F}_k(x, y, m)$ is the climatology of ECCO adjustments:

$$\tilde{F}_k(x, y, m) = \frac{1}{N_{\text{yr}}} \sum_{i=1}^{N_{\text{yr}}} [F_k^{\text{ECCO}}(x, y, [i-1] \times 12 + m) - F_k^{\text{ERA}}(x, y, [i-1] \times 12 + m)].$$

Here, $F_k^{\text{ECCO}}(x, y, t)$ is the atmospheric state variable from the ECCOv4r2 optimization from the t th month in 1992–2011 and $N_{\text{yr}} = 20$. This provides an additional 13 years of forcing to the model start and end dates.

REFERENCES

- Ansorge, I. J., and Coauthors, 2014: Basin-wide oceanographic array bridges the South Atlantic. *Eos, Trans. Amer. Geophys. Union*, **95**, 53–54, <https://doi.org/10.1002/2014EO060001>.
- Biastoch, A., C. W. Böning, and J. R. E. Lutjeharms, 2008: Agulhas leakage dynamics affects decadal variability in Atlantic overturning circulation. *Nature*, **456**, 489–492, <https://doi.org/10.1038/nature07426>.
- Bugnon, V., C. Hill, and P. H. Stone, 2006: An adjoint analysis of the meridional overturning circulation in an ocean model. *J. Climate*, **19**, 3732–3750, <https://doi.org/10.1175/JCLI3787.1>.
- Cunningham, S. A., and Coauthors, 2007: Temporal variability of the Atlantic meridional overturning circulation at 26.5°N. *Science*, **317**, 935–938, <https://doi.org/10.1126/science.1141304>.
- Czeschel, L., D. P. Marshall, and H. L. Johnson, 2010: Oscillatory sensitivity of Atlantic overturning to high-latitude forcing. *Geophys. Res. Lett.*, **37**, L10601, <https://doi.org/10.1029/2010GL043177>.
- Dee, D. P., and Coauthors, 2011: The ERA-Interim reanalysis: Configuration and performance of the data assimilation system. *Quart. J. Roy. Meteor. Soc.*, **137**, 553–597, <https://doi.org/10.1002/qj.828>.
- Dong, S., S. Garzoli, M. Baringer, C. Meinen, and G. Goni, 2009: Interannual variations in the Atlantic meridional overturning circulation and its relationship with the net northward heat transport in the South Atlantic. *Geophys. Res. Lett.*, **36**, L20606, <https://doi.org/10.1029/2009GL039356>.
- , —, and —, 2011: The role of interocean exchanges on decadal variations of the meridional heat transport in the South Atlantic. *J. Phys. Oceanogr.*, **41**, 1498–1511, <https://doi.org/10.1175/2011JPO4549.1>.
- , M. O. Baringer, G. J. Goni, C. S. Meinen, and S. L. Garzoli, 2014: Seasonal variations in the South Atlantic meridional overturning circulation from observations and numerical models. *Geophys. Res. Lett.*, **41**, 4611–4618, <https://doi.org/10.1002/2014GL060428>.
- , G. Goni, and F. Bringas, 2015: Temporal variability of the South Atlantic meridional overturning circulation between 20°S and 35°S. *Geophys. Res. Lett.*, **42**, 7655–7662, <https://doi.org/10.1002/2015GL065603>.
- Ducet, N., P. Y. Le Traon, and G. Reverdin, 2000: Global high-resolution mapping of ocean circulation from TOPEX/Poseidon and ERS-1 and -2. *J. Geophys. Res.*, **105**, 19 477–19 498, <https://doi.org/10.1029/2000JC900063>.
- Farneti, R., and T. L. Delworth, 2010: The role of mesoscale eddies in the remote oceanic response to altered Southern Hemisphere winds. *J. Phys. Oceanogr.*, **40**, 2348–2354, <https://doi.org/10.1175/2010JPO4480.1>.
- Fekete, B. M., C. J. Vörösmarty, and W. Grabs, 2002: High-resolution fields of global runoff combining observed river discharge and simulated water balances. *Global Biogeochem. Cycles*, **16**, 1042, <https://doi.org/10.1029/1999GB001254>.
- Fetter, A. F. H., and R. P. Matano, 2008: On the origins of the variability of the Malvinas Current in a global, eddy-permitting numerical simulation. *J. Geophys. Res.*, **113**, C11018, <https://doi.org/10.1029/2008JC004875>.
- Forget, G., J.-M. Campin, P. Heimbach, C. N. Hill, R. M. Ponte, and C. Wunsch, 2015a: ECCO version 4: An integrated framework for non-linear inverse modeling and global ocean state estimation. *Geosci. Model Dev.*, **8**, 3071–3104, <https://doi.org/10.5194/gmd-8-3071-2015>.
- , D. Ferreira, and X. Liang, 2015b: On the observability of turbulent transport rates by Argo: Supporting evidence from an inversion experiment. *Ocean Sci.*, **11**, 839–853, <https://doi.org/10.5194/os-11-839-2015>.
- , J.-M. Campin, P. Heimbach, C. N. Hill, R. M. Ponte, and C. Wunsch, 2016: ECCO version 4: Second release. Massachusetts Institute of Technology Tech. Rep., 147 pp., <http://hdl.handle.net/1721.1/102062>.
- Garzoli, S. L., and R. Matano, 2011: The South Atlantic and the Atlantic meridional overturning circulation. *Deep-Sea Res. II*, **58**, 1837–1847, <https://doi.org/10.1016/j.dsr2.2010.10.063>.
- , M. O. Baringer, S. Dong, R. C. Perez, and Q. Yao, 2013: South Atlantic meridional fluxes. *Deep-Sea Res. I*, **71**, 21–32, <https://doi.org/10.1016/j.dsr.2012.09.003>.
- Gaspar, P., Y. Grégoris, and J.-M. Lefevre, 1990: A simple eddy kinetic energy model for simulations of the oceanic vertical mixing: Tests at station Papa and long-term upper ocean study site. *J. Geophys. Res.*, **95**, 16 179–16 193, <https://doi.org/10.1029/JC095iC09p16179>.
- Gent, P. R., and J. C. McWilliams, 1990: Isopycnal mixing in ocean circulation models. *J. Phys. Oceanogr.*, **20**, 150–155, [https://doi.org/10.1175/1520-0485\(1990\)020<0150:IMOCM>2.0.CO;2](https://doi.org/10.1175/1520-0485(1990)020<0150:IMOCM>2.0.CO;2).
- , and G. Danabasoglu, 2011: Response to increasing Southern Hemisphere winds in CCSM4. *J. Climate*, **24**, 4992–4998, <https://doi.org/10.1175/JCLI-D-10-05011.1>.
- Giering, R., T. Kaminski, and T. Slawig, 2005: Generating efficient derivative code with TAF: Adjoint and tangent linear Euler flow around an airfoil. *Future Gener. Comput. Syst.*, **21**, 1345–1355, <https://doi.org/10.1016/j.future.2004.11.003>.
- Heimbach, P., C. Hill, and R. Giering, 2005: An efficient exact adjoint of the parallel MIT general circulation model, generated

- via automatic differentiation. *Future Gener. Comput. Syst.*, **21**, 1356–1371, <https://doi.org/10.1016/j.future.2004.11.010>.
- , D. Menemenlis, M. Losch, J.-M. Campin, and C. Hill, 2010: On the formulation of sea-ice models. Part 2: Lessons from multi-year adjoint sea-ice export sensitivities through the Canadian Arctic Archipelago. *Ocean Modell.*, **33**, 145–158, <https://doi.org/10.1016/j.ocemod.2010.02.002>.
- , C. Wunsch, R. M. Ponte, G. Forget, C. Hill, and J. Utke, 2011: Timescales and regions of the sensitivity of Atlantic meridional volume and heat transport: Toward observing system design. *Deep-Sea Res. II*, **58**, 1858–1879, <https://doi.org/10.1016/j.dsr2.2010.10.065>.
- Huffman, G. J., and Coauthors, 1997: The Global Precipitation Climatology Project (GPCP) combined precipitation dataset. *Bull. Amer. Meteor. Soc.*, **78**, 5–20, [https://doi.org/10.1175/1520-0477\(1997\)078<0005:TGPCPG>2.0.CO;2](https://doi.org/10.1175/1520-0477(1997)078<0005:TGPCPG>2.0.CO;2).
- Johnson, H. L., and D. P. Marshall, 2002a: A theory for the surface Atlantic response to thermohaline variability. *J. Phys. Oceanogr.*, **32**, 1121–1132, [https://doi.org/10.1175/1520-0485\(2002\)032<1121:ATFTSA>2.0.CO;2](https://doi.org/10.1175/1520-0485(2002)032<1121:ATFTSA>2.0.CO;2).
- , and —, 2002b: Localization of abrupt change in the North Atlantic thermohaline circulation. *Geophys. Res. Lett.*, **29**, 1083, <https://doi.org/10.1029/2001GL014140>.
- , and —, 2004: Global teleconnections of meridional overturning circulation anomalies. *J. Phys. Oceanogr.*, **34**, 1702–1722, [https://doi.org/10.1175/1520-0485\(2004\)034<1702:GTOMOC>2.0.CO;2](https://doi.org/10.1175/1520-0485(2004)034<1702:GTOMOC>2.0.CO;2).
- Köhl, A., 2005: Anomalies of meridional overturning: Mechanisms in the North Atlantic. *J. Phys. Oceanogr.*, **35**, 1455–1472, <https://doi.org/10.1175/JPO2767.1>.
- Large, W. G., and S. Yeager, 2004: Diurnal to decadal global forcing for ocean and sea-ice models: The data sets and flux climatologies. NCAR Tech. Note NCAR/TN-460+STR, 105 pp., <https://doi.org/10.5065/D6KK98Q6>.
- Lopez, H., G. Goni, and S. Dong, 2017: A reconstructed South Atlantic meridional overturning circulation time series since 1870. *Geophys. Res. Lett.*, **44**, 3309–3318, <https://doi.org/10.1002/2017GL073227>.
- Losch, M., D. Menemenlis, J.-M. Campin, P. Heimbach, and C. Hill, 2010: On the formulation of sea-ice models. Part 1: Effects of different solver implementations and parameterizations. *Ocean Modell.*, **33**, 129–144, <https://doi.org/10.1016/j.ocemod.2009.12.008>.
- Lozier, M. S., and Coauthors, 2017: Overturning in the Subpolar North Atlantic Program: A new international ocean observing system. *Bull. Amer. Meteor. Soc.*, **98**, 737–752, <https://doi.org/10.1175/BAMS-D-16-0057.1>.
- Marotzke, J., R. Giering, K. Q. Zhang, D. Stammer, C. Hill, and T. Lee, 1999: Construction of the adjoint MIT ocean general circulation model and application to Atlantic heat transport sensitivity. *J. Geophys. Res.*, **104**, 29 529–29 547, <https://doi.org/10.1029/1999JC900236>.
- Marshall, J., A. Adcroft, C. Hill, L. Perelman, and C. Heisey, 1997: A finite-volume, incompressible Navier Stokes model for studies of the ocean on parallel computers. *J. Geophys. Res.*, **102**, 5753–5766, <https://doi.org/10.1029/96JC02775>.
- Matano, R. P., C. G. Simionato, and P. T. Strub, 1999: Modeling the wind-driven variability of the south Indian Ocean. *J. Phys. Oceanogr.*, **29**, 217–230, [https://doi.org/10.1175/1520-0485\(1999\)029<0217:MTWDVO>2.0.CO;2](https://doi.org/10.1175/1520-0485(1999)029<0217:MTWDVO>2.0.CO;2).
- , E. J. Beier, P. T. Strub, and R. Tokmakian, 2002: Large-scale forcing of the Agulhas variability: The seasonal cycle. *J. Phys. Oceanogr.*, **32**, 1228–1241, [https://doi.org/10.1175/1520-0485\(2002\)032<1228:LSFOTA>2.0.CO;2](https://doi.org/10.1175/1520-0485(2002)032<1228:LSFOTA>2.0.CO;2).
- Meinen, C. S., and Coauthors, 2013: Temporal variability of the meridional overturning circulation at 34.5°S: Results from two pilot boundary arrays in the South Atlantic. *J. Geophys. Res. Oceans*, **118**, 6461–6478, <https://doi.org/10.1002/2013JC009228>.
- Menemenlis, D., and Coauthors, 2005: NASA supercomputer improves prospects for ocean climate research. *Eos, Trans. Amer. Geophys. Union*, **86**, 89–96, <https://doi.org/10.1029/2005EO090002>.
- Pillar, H. R., 2013: Sensitivity of the Atlantic meridional overturning circulation to surface forcing. Ph.D. thesis, University of Oxford, 274 pp., <https://ora.ox.ac.uk/objects/uuid:42366dc7-e699-4349-95d2-89a97033d957>.
- , P. Heimbach, H. L. Johnson, and D. P. Marshall, 2016: Dynamical attribution of recent variability in Atlantic overturning. *J. Climate*, **29**, 3339–3352, <https://doi.org/10.1175/JCLI-D-15-0727.1>.
- Rayner, D., and Coauthors, 2011: Monitoring the Atlantic meridional overturning circulation. *Deep-Sea Res. II*, **58**, 1744–1753, <https://doi.org/10.1016/j.dsr2.2010.10.056>.
- Redi, M. H., 1982: Oceanic isopycnal mixing by coordinate rotation. *J. Phys. Oceanogr.*, **12**, 1154–1158, [https://doi.org/10.1175/1520-0485\(1982\)012<1154:OIMBCR>2.0.CO;2](https://doi.org/10.1175/1520-0485(1982)012<1154:OIMBCR>2.0.CO;2).
- Risien, C. M., and D. B. Chelton, 2008: A global climatology of surface wind and wind stress fields from eight years of QuikSCAT scatterometer data. *J. Phys. Oceanogr.*, **38**, 2379–2413, <https://doi.org/10.1175/2008JPO3881.1>.
- SAMOC Initiative, 2017: South Atlantic meridional overturning circulation (SA MOC). NOAA, <http://www.aoml.noaa.gov/phod/SAMOC>.
- Wunsch, C., and P. Heimbach, 2007: Practical global oceanic state estimation. *Physica D*, **230**, 197–208, <https://doi.org/10.1016/j.physd.2006.09.040>.
- , and —, 2013a: Dynamically and kinematically consistent global ocean circulation and ice state estimates. *Ocean Circulation and Climate*, G. Siedler et al., Eds., International Geophysics Series, Vol. 103, Academic Press, 553–579, <https://doi.org/10.1016/B978-0-12-391851-2.00021-0>.
- , and —, 2013b: Two decades of the Atlantic meridional overturning circulation: Anatomy, variations, extremes, prediction, and overcoming its limitations. *J. Climate*, **26**, 7167–7186, <https://doi.org/10.1175/JCLI-D-12-00478.1>.
- Yeager, S., and G. Danabasoglu, 2014: The origins of late-twentieth-century variations in the large-scale North Atlantic circulation. *J. Climate*, **27**, 3222–3247, <https://doi.org/10.1175/JCLI-D-13-00125.1>.